

Review

Graphene and Graphene Nanomesh Spintronics

Junji Haruyama

Faculty of Science and Engineering, Aoyama Gakuin University, 5-10-1 Fuchinobe, Sagamiara, Kanagawa 252-5258, Japan; E-Mail: J-haru@ee.aoyama.ac.jp; Tel./Fax: +81-42-759-6256

Received: 11 September 2013; in revised form: 25 October 2013 / Accepted: 5 November 2013 /

Published: 4 December 2013

Abstract: Spintronics, which manipulate spins but not electron charge, are highly valued as energy and thermal dissipationless systems. A variety of materials are challenging the realization of spintronic devices. Among those, graphene, a carbon mono-atomic layer, is very promising for efficient spin manipulation and the creation of a full spectrum of beyond-CMOS spin-based nano-devices. In the present article, the recent advancements in graphene spintronics are reviewed, introducing the observation of spin coherence and the spin Hall effect. Some research has reported the strong spin coherence of graphene. Avoiding undesirable influences from the substrate are crucial. Magnetism and spintronics arising from graphene edges are reviewed based on my previous results. In spite of carbon-based material with only sp^2 bonds, the zigzag-type atomic structure of graphene edges theoretically produces spontaneous spin polarization of electrons due to mutual Coulomb interaction of extremely high electron density of states (edge states) localizing at the flat energy band. We fabricate honeycomb-like arrays of low-defect hexagonal nanopores (graphene nanomeshes; GNMs) on graphenes, which produce a large amount of zigzag pore edges, by using a nonlithographic method (nanoporous alumina templates) and critical temperature annealing under high vacuum and hydrogen atmosphere. We observe large-magnitude ferromagnetism, which arises from polarized spins localizing at the hydrogen-terminated zigzag-nanopore edges of the GNMs, even at room temperature. Moreover, spin pumping effects are found for magnetic fields applied in parallel with the few-layer GNM planes. Strong spin coherence and spontaneously polarized edge spins of graphene can be expected to lead to novel spintronics with invisible, flexible, and ultra-light (wearable) features.

Keywords: spintronics; graphene; edges; spin polarization; ferromagnetism; magnetoresistance; rare-metal free

1. Introduction

Spintronics are highly promising as a key technology for next generation [1–7]. They have the following two prospects: (1) Zero-emission energy and (2) replacement of CMOS technology (*i.e.*, beyond CMOS). From the first prospect, electron spin currents carry and emit no energy and no heat. This strong advantage resolves heat problems in large-scale integration circuits, personal computers, and also any systems loading them. In particular, heat problems become much more significant in highly closed spaces (e.g., on aerospace and air planes). Spintronic devices and circuits must be extremely effective for such systems. From the second viewpoint, it is a desirable subject for human life to realize devices beyond CMOS FETs, which are approaching its integration and operation limits. Although many materials and technologies have challenged this, it has not yet been realized. Spintronic devices based on some kinds of ideas must realize this. For instance, operation utilizing spin flipping leads to extremely high switching devices (e.g., in pico-seconds), which overcomes operation speeds of CMOS FETs and LSIs. Spin quantum bits also enable the treatment of large amounts of information by much smaller-scale integration compared to CMOS circuits. Therefore, spintronic devices are desired as future key technology.

Some kinds of structures have been developed for spintronics [1–7], such as giant magnetoresistance (GMR) [1], tunneling MR (TMR) [2,3], and spin-valve structures. In particular, TMR structure has realized high efficiency of TMR ratio. Even TMR ratio of as high as over 1000% has been obtained by using CoFeB/MgO/CoFeB junction [4]. Spintronic devices have also been based on a variety of materials, e.g., ferromagnetic metals (e.g., cobalt (Co), iron (Fe), chromium (Cr), manganese (Mn)) [1–4] and ferromagnetic semiconductors ((In, Mn), As) *etc.* [5–7]).

On the other hand, graphene, a carbon mono-atomic layer, has recently emerged followed by the discovery of an easy fabrication method, the so-called mechanical exfoliation of graphite. The field rapidly grew, and a Nobel Prize was awarded in 2010 for work related to this fabrication method. Here, strong spin coherence has been highly expected in graphene because of the weak spin-orbit interaction (SOI) and weak hyperfine interaction, which are unique to carbon atoms. Some works, however, reported on the weak spin coherence and the origins arising from substrate, impurities, and so on [8,9], while other works reported on the strong coherence, as predicted by theories [10,11]. Thus, the issue is still under debate. What is certain is that there exist undesirable influences originating from the substrate on the spin coherence, such as ripples, impurities, and defects. Because graphene is a mono-atomic layer directly fabricated on substrates, such factors significantly and certainly suppress the spin coherence. Avoiding these factors (e.g., by utilizing a hexagonal-boron-nitride (h-BN) substrate [12]) enables the fabrication of highly effective spintronic devices with a strong spin coherence.

As a recent exciting topic, phenomena associated with spin Hall Effect (SHE) [13] in graphenes have been recently reported. Realization of (quantum) SHE was theoretically predicted by resolving double degeneration of spin bands (e.g., by introducing spin orbit interaction (SOI)) and controlling

two spins with opposite moments existing in different two bands only by applying electric fields [13–16]. Experimentally, observation of large spin diffusion current examined from a SHE-like method in high-quality graphenes on h-BN [12] and also pure SHE in hydrogenated graphenes with introducing SOI [17] has been recently confirmed. They are opening a door to novel all-carbon spintronics.

Moreover, in any of the spintronic devices mentioned above, rare magnetic elements are indispensable in order to provide polarized spins to the systems. In contrast, from a theoretical viewpoint, it is known that carbon-based sp^x -orbital systems can lead to the spontaneous emergence of electron spin polarization based on edge-localized electrons [18–24]. In particular, zigzag-atomic structure at graphene edges has been attracted nontrivial attention [18–23,25–43]. The following two models predicted it.

One is the graphene nanoribbon (GNR) model, which assumes perfect edge atomic structures without any defects. It allows that the electron spins localizing at zigzag edges [18] to become stabilized toward polarization (*i.e.*, (anti)ferromagnetism) due to the exchange interaction between the two edges. This produces a maximum spin ordering in this orbital, in a GNR that is an one-dimensional strip line of graphene with edges on both longitudinal sides [18–24], in graphene nanomeshes (GNMs) with hexagonal nanopore arrays (Figure 1) [28,39] and in graphene nanoflakes [29]. This is similar to the case of Hund's rule for atoms. Moreover, spin configuration depends on kinds and number of foreign atoms (e.g., hydrogen (H) and oxygen (O)), which terminate edge carbon dangling bonds [20,41].

The other model is the so-called Lieb's theorem. Following it, the presence of low-concentration defects in ensemble of carbon atoms (e.g., graphene flakes) results in the appearance of net magnetism. It predicts the emergence of ferromagnetism by an increase in the difference between the number of removed A and B sites (Δ_{AB}) of the graphene bipartite lattice at zigzag edges [39,41]. The magnitude of ferromagnetism increases with increasing values of Δ_{AB} .

Although there are many reports for defect-based magnetism in graphene [44–46], very few experimental reports exist for purely zigzag-edge-derived magnetism. My group has successfully reported on observation of the edge polarized spins, ferromagnetism, and spin-based phenomena arising from zigzag pore edges by fabricating low-defect hydrogenated GNMs by a non-lithographic method [42,43]. Utilizing graphene edges spins leads to novel spintronic devices. For instance, the spin-filtering effect predicted that GNRs with antiferromagnetic spin alignment on two edges can only manipulate electron spins with the same moment and that the electron spins can be controlled by applying in-plane electric fields [18].

In the present manuscript, recent experimental advancement of spin-based phenomena in graphenes is reviewed in Section 2.1. Then, my group's previous experimental results about edge spins are reviewed in section 2.2.

2. Recent Experimental Advancement of Spin-Based Phenomena in Graphenes

2.1. Advancement of Graphen Spintronics

2.1.1. Spin Coherence in Graphene

A large spin coherence length ($\gg 1 \mu\text{m}$) and time ($\gg 1 \text{ms}$) are expected for graphene, which allow for the realization of novel spintronic devices with a long lifetime and operation at room temperature.

From a theoretical viewpoint, the following two causes are at least considered as the origin of the strong spin coherence in graphene: (1) the absence of the SOI due to the small mass of the carbon atom and (2) the weak hyperfine interaction due to the absence of the nuclear spins of the carbon nuclei (only 1% of the nuclei are ^{13}C and have spin). These causes are significantly different from those in other magnetic material systems (e.g., magnetic compound semiconductors and magnetic metals) consisting of heavy-mass atoms.

However, the spin lifetime (e.g., <1 ns) actually observed in some works is far from the predicted value, and the reasons for this observation have been discussed. For instance, ripples in the substrate, vacancies and adatoms may introduce non-uniform and local electric fields, resulting in the appearance of the SOI and the short spin lifetime. Charged impurities in the substrate and remote surface phonons may also weaken the spin coherence. Moreover, magnetic and paramagnetic defects may couple with the conducting spins and suppress the spin coherence. In order to clarify the origins, ref. [8] carried out the following well-known two quantum interference measurements, which are observed when the phase coherence length (l_ϕ) is comparable to the device dimensions and disentangle the sources of magnetic and nonmagnetic decoherence: (1) universal conductance fluctuations (UCF) in which the dynamic conductance is quantized to a universal value independent of the sample size and geometrical scattering factors. Their statistics (e.g., fluctuation magnitude and dephasing rate) follow the theoretical predictions and are also determined by the magnetic dephasing mechanism; (2) Weak localization (WL) produces a maximum resistance and results in Anderson localization when the device size is much smaller than l_ϕ . The WL fits to the average low-field magnetoconductance, which is determined only by nonmagnetic dephasing in graphene. The experiment combined UCF and WL measurements to separate and quantify the various sources of dephasing in graphene and revealed that both magnetic and nonmagnetic dephasing mechanisms limit the coherence in graphene below 1 K. The magnetic scattering rate was too large to be explained by remote magnetic moments, instead requiring that the magnetic defects are electronically coupled to graphene. Therefore, magnetic defects are the primary cause of spin relaxation, masking any potential effects of the SOI. Although the origins for magnetic defects in graphene were not clarified, it is quite important that the experiment revealed that magnetic defects are the dominant factor for spin decoherence.

The technique of pulsed electron spin resonance (ESR) spectroscopy is also useful [9,47] because it can avoid the influence of the electrode contacts on spin coherence. ESR spectroscopy can reveal the nature of edge spins and spin dynamics in detail through a broad multifrequency continuous wave. ESR experiments on pristine free-standing GNRs in [9] led to spin relaxation times on the order of microseconds and also discovered that the spin relaxation times are strongly temperature dependent, unlike the weak temperature dependence theoretically predicted. It was concluded that the spin relaxation times are determined by a tunneling level state-type relaxation process, typically observed for disordered materials in which the defect paramagnetic centers are not strongly bound to the main phonon bath, indicating that the phonon contribution is negligible in free-standing GNRs. On the basis of the data, it ruled out the undesirable contributions originating from the charged impurities in a substrate (causing strong impurity Coulomb scattering that limits the spin relaxation rate), as the GNRs are free-standing without being supported by an underlying substrate. This report also proved the above-mentioned causes arising from substrates for the suppression of spin coherence.

In contrast, some works reported on the spin coherence of graphene. For example, ref. [10] reported a spin coherence length as large as 2 μm and a spin coherence time as long as 150 ps at room temperature via non-local spin-valve measurements with Co electrodes on mono-layer graphene with an electron mobility of 2000 cm^2/Vs . These results were extracted from the Hanle-type spin precession measurements. The spin polarization of the ferromagnetic contacts was also calculated from the measurements to be around 10%. The report also implied extrinsic impurity scattering as an origin for spin scattering.

Moreover, reference [11] reported on anisotropic spin relaxation in graphene by similar measurements using a non-local spin valve structure. A comparison of the spin signals at $B = 0$ and $B = 2$ T showed a 20% decrease in the spin relaxation time for spins perpendicular to the graphene layer (T_{\perp}) compared to spins parallel to the layer (T_{\parallel}). An analysis of the results was carried out in terms of the different strengths of the SO effective fields in the in-plane and out-of-plane directions. For example, if the SOI is of the Rashba or Dresselhaus type, the SO effective fields are exclusively in the graphene plane, and calculations showed that this should result in anisotropic spin relaxation in which $T_{\perp} = (1/2)T_{\parallel}$. On the other hand, if the SO effective fields pointing out of the graphene plane dominate, it is expected that $T_{\perp} \gg T_{\parallel}$. This corresponded to the experimental result. The report also discussed the role of the Elliott-Yafet mechanism, in which spin scattering is induced by electron (momentum) scattering from impurities, boundaries, and phonons, and the Dyakonov-Perel mechanism, which results from the SO terms in the Hamiltonian of the clean material, for spin relaxation. This provided quite useful information for spin scattering for the SOI.

Consequently, spin coherence in graphene is still under debate. However, as I have mentioned above, it is crucial to avoid undesirable influences from the substrate on the spin coherence, which has been successfully realized by utilizing an h-BN substrate, which has very weak interaction with the graphene fabricated on it. In the next section, an example is considered in more detail.

2.1.2. Spin Hall Effect

The SHE is a phenomenon typically observed in a topological insulator [13–16] in which the electron spins are strongly preserved owing to topological reasons (e.g., the presence of the SOI), and the spin relaxation time is determined only by the uncertainty principle between energy and time. The SOI resolves the double degeneration of the energy bands and the opposite-moment spins (up and down moments) existing in the different two bands run toward opposite directions under applied electric fields, resulting in the appearance of the SHE. Thus, one can produce and control the Hall effect and spin currents without applying magnetic fields.

Two evident works associated with SHE in graphenes have been recently reported as mentioned above. One is the large spin diffusion current observed in SHE-like method in high-quality graphenes fabricated on h-BN substrate [12], while the other is observation of the intrinsic SHE in hydrogenated graphenes with introducing large SOI [17].

The former was observed in high-quality graphenes with electron mobility as high as $\sim 150,000$ cm^2/Vs on h-BN substrate. It is well known that there is very weak interaction between h-BN and graphenes, resulting in less influence of substrate to the suppression of spin coherence mentioned above. It revealed true potential of graphenes similarly to the case of suspended graphenes. The experiments were carried out using electron spins with opposite moments, which are located in two

different bands that were formed by Zeeman splitting. Making a constant current flow between two probes in four probe patterns (Hall pattern) under magnetic field over Zeeman energy, nonlocal resistance (R_{NL}) between other two probes was observed. Consequently, large peaks of R_{NL} were evidently confirmed, depending on temperature and magnetic fields. They could not be understood by conventional quantum Hall effect and could be rather similar to a SHE. The observed magnitude of the spin diffusion current was mostly 100 times greater than those in previous graphenes fabricated on conventional SiO_2 substrate. This strongly supports the relevance of the abovementioned origins for weak spin coherence caused by the interaction with substrate.

The result shows the true strong spin coherence of graphenes and also the high availability for spintronic devices. Quantum phenomena (e.g., fractional quantum Hall effect) in graphenes on h-BN substrate and also high electron motilities have been already reported, while reports of spin-based phenomenon are fewer in number. It reveals the essential natures of graphenes and enables an application to spintronic devices.

The latter observation of SHE was performed by terminating the individual carbon atoms of graphenes by hydrogen atoms. In the experiments, hydrogen silsesquioxane (HSQ) resist was used to precisely control a small amount of covalent H-termination of graphenes. After irradiation of the electron beam on the graphenes covered by HSQ, hydrogen atoms remained on the graphenes. As HSQ dose amount increases, the remaining amount of H-atoms increased linearly. After very weak hydrogenation $\sim 0.02\%$, they observed a significant increase in R_{NL} ($\sim 400\%$), well above what can be accounted for by R_{Ohmic} . With increasing hydrogenation, the measured R_{NL} showed a steep increase, reaching 170Ω at 0.05% hydrogenation. A strong increase of the R_{NL} was observed even at charge densities $> 1 \times 10^{12} \text{ cm}^{-2}$. As the ohmic contribution to R_{NL} remained negligible over the entire hydrogenation rate, they argued that the only plausible explanation for the observed R_{NL} increase was the SHE. Moreover, the SHE was confirmed by the non-monotonic oscillatory behavior of the non-local signal in an applied in-plane magnetic field and also by the length, width and adatom density dependence of the non-local signal. From the length dependence of the non-local signal, they extracted a spin relaxation length of $\sim 1 \mu\text{m}$, a spin relaxation time of $\sim 90 \text{ ps}$ and a SOI strength of $\sim 2.5 \text{ meV}$ for samples with 0.05% hydrogenation. The SOI strength is actually significantly higher than $\sim 10 \mu\text{eV}$ for conventional graphene with sp^2 orbitals.

The experiments, results, and analyses are quite interesting. The authors argued that an adatom locally breaks the reflection symmetry across the graphene plane, leading to an out-of-plane distortion by an angle ϕ relative to the plane (e.g., $\phi \approx 19.5^\circ$ for a full sp^3) and mixing σ and π orbitals that are no longer orthogonal. Hence, the SO interaction becomes a first-order effect leading to a large enhancement of SO coupling for covalently bonded hydrogen impurities in graphene. However, the following questions still remain; (1) Why can carbon and hydrogen atoms with small mass lead to strong SOI? (2) How are the surface carbon atoms of bulk graphene covalently hydrogenated with the best angle for SP^3 orbitals? (3) How are the edge states and termination of edge dangling bonds correlated with the strong SOI?

From (1), even with formation of the sp^3 hybrid orbitals and out-of-plane distortion, the masses of hydrogen and carbon may be too small compared to heavy masses in conventional SOI cases. From (2), due to distortion and rippling from substrate, it seems to be hard to hydrogenate bulk graphenes with the best angle to form sp^3 orbitals. Why such C–H bonds were automatically formed remained in

question. In this viewpoint, correlation of the edge dangling bonds is not clear for (3). Because the width of the graphenes used for the experiments are $\sim 1 \mu\text{m}$, they are not GNRs. Nevertheless, di-hydrogenation of the edge dangling bonds easily forms sp^3 orbitals compared to those in bulk. Thus, it is indispensable to reveal its contribution.

In any cases, these reports of the large spin diffusion currents of graphenes on h-BN substrate and the SHE realized by strong SOI in hydrogenated graphenes suggest high feasibility of graphene spins to novel spintronics. They must open a door to (magnetic-atom-free) carbon spintronics by manipulating electron spins by applying electric fields, after further investigation and development.

2.2. Magnetism and Spintronics on Pore Edge Spins in Graphene Nanomeshes

Many works have reported on magnetism arising from defects in graphene [44–46]. In contrast, very few works have experimentally reported on observation of magnetism and spin-based phenomena to truly arise from graphene zigzag edges. This is because edge-related phenomena are easily destroyed by disorder (damage, defects) and contamination introduced during the fabrication process (e.g., by lithographic methods). We have, therefore, developed two non-lithographic fabrication methods for low-defect graphene edges; (1) GNRs derived from unzipping of carbon nanotubes combined with air blow and three-step annealing [32] and (2) GNMs fabricated using nano-porous alumina template (NPAT) [42,43]. In the present section, observation of magnetism and spin-related phenomena are reviewed based on the latter one.

2.2.1. Ferromagnetism Arising from Zigzag-Type Pore Edges

2.2.1.1. Sample Fabrication for GNMs

GNMs, which have honeycomb-like array of hexagonal nanopores (Figure 1b,e), were fabricated on a large ensemble of mechanically exfoliated graphenes (or graphenes CVD-synthesized on SiC substrate) by using NPAT (Figure 1a) [48] as an etching mask (Figure 1c), following our previous nonlithographic method [27,36]. The NPAT is easily fabricated through self-organization by anodic oxidation of pure (99.99%) aluminum films. The graphene was carefully etched by optimized low-power Ar gas (e.g., 200–600 V for 10–40 min) so as to avoid giving damages (Figure 1d) and the naomesh of the NPAT was transferred to graphene. Then, the NPAT was detached from the surface of the fabricated GNM, either mechanically or chemically.

All the GNMs fabricated through these processes (including Figure 2c,f sample) were annealed at 800 °C in high vacuum (10^{-6} Torr) for 0.5–3 days with continual pumping of gas and, then, in hydrogen gas by the field-emission-type radical CVD system under pressure > 1 MPa at least for 3 h at for all the measurements. The first annealing is for deoxidization of the pore edges with recovering all damages and defects and is the key to forming zigzag pore edges by edge atomic reconstruction, while the second annealing is the key for termination of the carbon atoms at the pore edges by hydrogen atoms.

For observation of the features shown in Figure 2b,e, after the observation of the feature in Figure 2a, the sample was annealed at 800 °C in high vacuum (10^{-6} Torr) for 3 days with continual pumping of gas for de-hydrogenation of the edges and, then, in oxygen atmosphere for 1 h for oxidization of the pore edges. Magnetization measurements were carried out directly after the annealing.

Figure 1. (a) SEM top view of a nano-porous alumina template (NPAT), which shows honeycomb-like array of hexagonal nano-pores; (b) AFM image of a graphene nanomesh (GNM) transferred following (c) and (d), which also proves the hexagonal shape of the pores (mean diameter $\phi \sim 80$ nm and mean inter-pore distance $W \sim 20$ nm); (c,d) Schematic cross sectional views of nonlithographic fabrication process of a GNM; (c) NPAT was placed on graphene as an etching mask; (d) The graphene is carefully etched by Ar gas, resulting in formation of a GNM; (e) Schematic view of a GNM with the zigzag-type pore-edge. Interpore regions can correspond to GNRs. Actual interpore regions include a larger number of hexagonal carbon unit cells per inter-pore region with length ~ 40 nm and $W \sim 20$ nm. This GNM structure brings at least three large advantages as mentioned in the text.

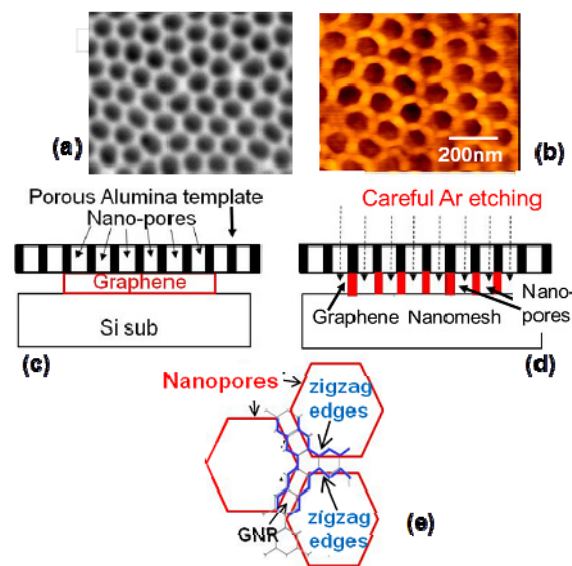
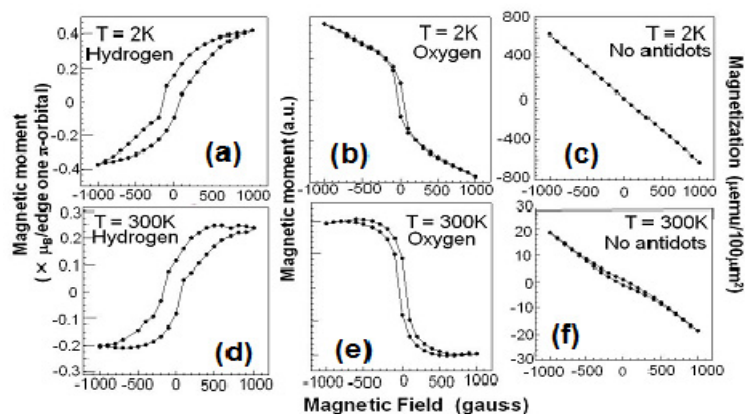


Figure 2. Magnetization of monolayer GNMs with $\phi \sim 80$ nm and $W \sim 20$ nm for termination of different atoms. (a,d) hydrogen-terminated pore edges; (b,e) oxygen-terminated pore edges; and (c,f) bulk graphene without pore arrays. DC magnetization was measured by a superconducting quantum interference device (SQUID; Quantum Design). Magnetic fields were applied perpendicular to GNMs. The vertical axis in panels (a) and (d) denote magnetic moment per localized-edge π orbital, assuming mono-hydrogenation of individual edge carbon atoms as explained in text.



This method brings at least the following three significant benefits. (1) It gives fewer defects and contamination to the nanopore edges of GNMs because of the non-lithographic method; (2) The honeycomb-like array of hexagonal nanopores can result in the formation of a large ensemble of GNRs and pore edges with sufficient lengths (e.g., 40 nm in the present case), because one hexagonal nanopore can have six edges and the inter-pore regions can correspond to GNRs (Figure 1e). In the actual GNM, it is speculated that mixture of zigzag and armchair edges exists in one inter-pore GNR (one pore edge), as reported by previous STM observation [49]. Even so, a large number of GNRs in the present GNMs can yield a large area of assembled zigzag-edge GNRs. This is extremely effective in detecting small magnetic and electric signals arising from the pore edges; (3) When one would align the atomic structure of one pore edge to zigzag, the other five pore edges can automatically have zigzag atomic structure from a topological reason. At the current stage, this is impossible and we unintentionally form zigzag pore edges only via critical-temperature annealing, unlike in [35].

We have no direct evidence for the presence of zigzag-type pore edges. In [42], however, we indirectly proved presence of zigzag atomic structure at the pore edges by observation of the highly suppressed ratios of D/G peak heights (<0.2) in Raman spectroscopy, which were realized by reconstruction of edge atomic structure to zigzag type by the critical-temperature annealing. Indeed, at least two other groups reported similar correlation previously in intentionally fabricated zigzag-edged hexagonal nanopores [35] and also graphene flakes [40]. Conventionally, low D/G peak ratios can be evidence for low defects in samples. In contrast, they can also be evidence for zigzag pore edges when one dimensionality of the edges is taken into account [40].

As mentioned above, we could not intentionally form zigzag-type pore-edge atomic structure (e.g., using the advantage (3) mentioned above). In [30,31], however, it is suggested that the zigzag edge is the most stable chemically and that arm chair-based edges are reconstructed to zigzag after STM Joule heating for long edges of overlapped graphenes [30] and electron beam (EB) irradiation for pore edges [31]. This stability may be simply understood by the difference in the number of carbon atoms bonded to two neighboring carbon atoms (dangling bonds) for the zigzag edge (*i.e.*, one such atom) and arm chair edges (two such atoms) [31]. After removal of such atoms, the arm chair edge requires energy two-times larger than zigzag in order to repair the removed atoms and, thus, becomes unstable. In our system, we carried out high-temperature annealing for narrow ($W \sim 20$ nm) GNRs (*i.e.*, narrow inter-pore spacing). This should bring the energy similar to that in [30,31] and cause the reconstruction of pore edge atomic structures to zigzag.

Moreover, the observed anomalous periodic-magnetoresistance (MR) oscillation also showed the presence of localized electrons at the pore edges in *H*-terminated GNMs [42]. This also supports the presence of the *H*-terminated zigzag-type pore edges [42].

2.2.1.2. Magnetism on Pore Edge Termination by Different Foreign Atoms

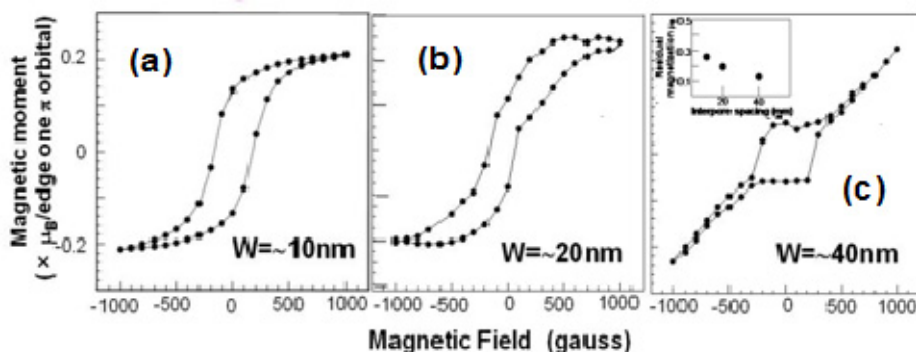
The results of magnetization measured for different-foreign-atom terminated monolayer GNM are shown in Figure 2. A ferromagnetic-hysteresis loop with large amplitude is clearly observed only in *H*-terminated samples in Figure 2a,d, which showed the low D/G peak ratio values (<0.2). In addition to this sample, three other samples with low D/G peak heights in Raman spectroscopy exhibited similar ferromagnetism. In contrast, *O*-terminated GNMs exhibit a diamagnetism-like weak hysteresis

loop (Figure 2b,e). This is consistent with [23], which reported that the formation of a spin-paired C–O chemical bond drastically reduces the local atomic magnetic moment of carbon at the zigzag edge of GNRs and suppresses the emergence of ferromagnetism.

Bulk graphenes without any pores and those assembled with NPATs show mostly no such features, even after H₂ annealing (Figure 2c,f), implying no contribution of parasitic factors (e.g., defects, impurities) of bulk graphenes. Moreover, the presence of fewer damages or impurities is reconfirmed in most the of bulk-graphene regions, because mechanically exfoliated bulk graphenes show an extremely low D/G peak heights ($\ll 0.1$) and a high 2D peak intensity in the Raman spectroscopy. These results strongly suggest that the observed ferromagnetism is associated with polarized spins localizing at the *H*-terminated zigzag-pore edges. It is surprising that the ferromagnetism observed at 2 K appears even at room temperature with a larger magnitude of the hysteresis loops (Figure 2d).

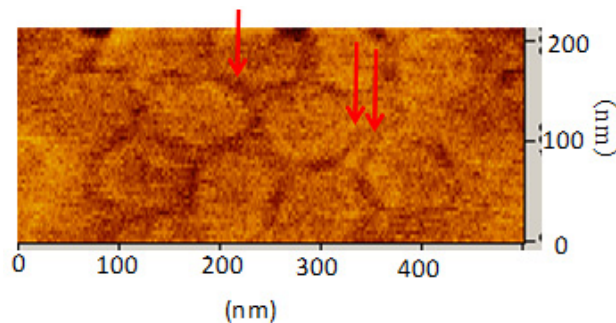
The correlation between the inter-pore spacing (corresponding to the width of the GNR, *W*; Figure 1e) and the magnetization is shown In Figure 3. It is found that the magnitude of hysteresis loop decreases with increasing *W*. In particular, it is revealed that the residual magnetization is inversely proportional to *W* value (inset of Figure 3c). This result is qualitatively consistent with the theories for the GNR model, according to which the edge spin stability and ordering of a zigzag-edge GNR are determined by the exchange interaction between the two edges, leading to vanishing of ferromagnetic edge spin ordering with increase of *W* [19,22]. Such a correlation cannot be understood by the ferromagnetism originating from the defects located only at pore edges or in the bulk graphene between pores. In the former case, ferromagnetism amplitude should be mostly independent of *W*, because defects are located only at pore edges. In the latter case, ferromagnetism amplitude should increase with an increase of *W*, because the density of the defects increases. Consequently, we conclude that the observed ferromagnetism is not due to parasitic origins (e.g., defects, impurities) but can be truly attributed to *H*-terminated zigzag pore edges.

Figure 3. Correlation of the observed ferromagnetism as a function of the mean inter-pore spacing *W* at *T* = 300 K. Mean pore diameter ($\phi \sim 80$ nm) was kept through all samples. For Figure 3a–c, difference in magnetic moment between upper and lower curves of hysteresis loop at *H* = 0 (residual magnetization $B_r \times 2$) is $\sim 0.28 \mu_B$, $\sim 0.2 \mu_B$, $\sim 0.12 \mu_B$ and the loop width at zero magnetic moment (coercivity $H_c \times 2$) is ~ 400 gauss, ~ 260 gauss, ~ 500 gauss, respectively. **Inset of (c);** B_r at 300 K as a function of *W*.



This is also consistent with MFM observation as shown in Figure 4. It clearly exhibits the presence of high density of polarized spins at the interpore GNR regions and also edge polarized spins at some pore edges. Because non-ferromagnetic samples show no such features, the observed ferromagnetism is attributed to these polarized spins. To date, approximately 50% of the samples, which include samples showing the low D/G peak heights, have shown ferromagnetism.

Figure 4. Magnetic force microscope (MFM) images of an H-terminated ferromagnetic GNM on SiC substrate. CoPtCr-coated Si probe was used for the measurements with a tapping mode. The interpore regions, which correspond to GNRs and exhibit darker color, imply high density of polarized spins. They directly suggest that the observed ferromagnetism originates from the GNRs. In particular, two arrows evidently imply the presence of edge polarized spins.



Disappearance of ferromagnetism in oxygen-terminated GNMs is interpreted as follows. Ref.[6] reported that the formation of a spin-paired C=O chemical bond drastically reduces the local atomic magnetic moment of carbon at the zigzag edge of GNRs and suppresses the emergence of ferromagnetism. The disappearance of ferromagnetism in Figure 2b,e is qualitatively consistent with this theory.

Moreover, in Figure 2b,e, even the diamagnetism of graphene mostly disappeared. One of the reasons for this is attributed to the formation of the nanomesh, because such an array drastically reduces the bulk graphene area available for the presence of loop currents to produce diamagnetism at the currently applied magnetic-field range (*i.e.*, corresponding to only GNRs with $W \sim 20$ nm between nanopores; Figure 1e). The radius of the cyclotron motion for electrons is given by $R_c = (\pi n_s)^{1/2} (h/2\pi) / eB$ [42]. By observing the magnetoresistance (*i.e.*, commensurability peak), we calculate n_s to be $\sim (4 \times 10^{11}) \text{ cm}^{-2}$ in the present GNMs. Based on this n_s value, R_c is calculated to be as large as ~ 400 nm, even for the currently applied largest magnetic field of 1000 gauss in Figure 2. Indeed, this R_c value is 20 times larger than $W \sim 20$ nm between the present nanopores, and it prohibits the emergence of loop currents for the formation of diamagnetism.

2.2.1.3. Theoretical Confirmation by Two Models: GNR Model and Lieb's Theorem

Here, two theoretical calculations quantitatively support our interpretation mentioned above. At first, employing the GNR model, which assumes pure zigzag pore edges (*i.e.*, without any defects) at all regions, enables the estimation of the magnetic moment of edge carbon atoms that contributes to the ferromagnetism observed in Figure 2. Assuming that only edge dangling bonds have localized spin

moments, the magnetic moment per edge dangling bond prior to H termination is estimated to be $(1.2 \times 10^{-23})/(\mu_B = 9.3 \times 10^{-24}) \sim 1.3 \mu_B$, where μ_B is the Bohr magneton, from the following.

The magnetic moment per edge dangling bond prior to H termination is estimated according to the following steps; (1) The total area of assembled bulk graphenes used for the pore array formation is $\sim 4 \text{ cm}^2$; (2) The area of one hexagonal unit cell with a pore is $S = 6(3^{-1/2}/2)(a/2)^2 \sim 4300 \text{ nm}^2$, where $a = [80 \text{ nm (pore diameter)} + 20 \text{ nm (interpore spacing)}]$; (3) Thus, the total number of pores is $(4 \text{ cm}^2)/(4300 \text{ nm}^2) \sim 10^{11} [(1)/(2)]$; (4) The total number of dangling bonds per hexagonal pore is $(40 \text{ nm})/(0.142 \text{ nm} \times 3^{1/2}) \times 6 = 166 \times 6 \sim 1000$; (5) The total number of edge dangling bonds of the GNM used for the SQUID measurement is $10^{14} [(3) \times (4)]$.

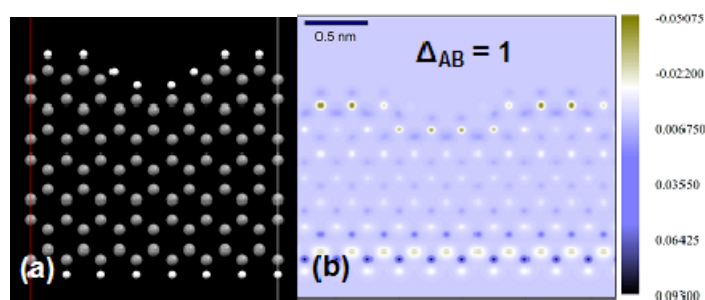
Therefore, using (5), the saturation magnetization per edge dangling bond is estimated to be $1.2 \times 10^{-6} (\text{emu}) \times 10^{-3}/10^{14} = 1.2 \times 10^{-23} (\text{J/T})$. Thus, the magnetic moment per edge dangling bond is estimated to be $(1.2 \times 10^{-23})/(\mu_B = 9.3 \times 10^{-24}) \sim 1.3 \mu_B$, where μ_B is the Bohr magneton. Conventionally, GNRs with no H -termination of dangling bonds should show antiferromagnetism, theoretically. However, in the above estimation, the observed total magnetization was divided by estimated number of edge dangling bonds in the GNM, leading us to neglect this theory.

Next, after H annealing at critical temperature, edge dangling bonds of a GNR are terminated by H atoms [3,5–7,9]. The following three types of H terminations are theoretically possible. (1) All edge dangling bonds are each terminated by one H atom on the side of both zigzag edges. It provides a flat band for $2\pi/3 \leq k \leq \pi$ in the Brillouin zone. Electrons are well localized at the edges; (2) Each of the edge dangling bonds on one side are terminated by two H atoms (so that the edge carbon atom becomes tetrahedrally coordinated; a bearded edge), while the dangling bonds on the opposite side are terminated by a single H atom. The GNR provides a flat band for $0 \leq k \leq \pi$, resulting in a completely localized “on-bonding state” around the Fermi level (E_F). This leads to the spin polarization of all carbon atoms; (3) The double H atom termination of the zigzag-edge carbon atoms on both sides of a GNR provides a flat band for $0 \leq k \leq 2\pi/3$ and creates a modified zigzag edge.

The type of edge H -termination could not be observed in the present experiment. However, our case should correspond to case (1) from the following reason. The mono- H termination of the edge dangling bond decreases its magnetic moment to one μ_B . The magnetic moment of one localized-edge π orbital is, therefore, estimated to be as large as $(\sim 1.3 \mu_B - 1 \mu_B) = \sim 0.3 \mu_B$. This is in fairly good agreement with the theoretical contribution of the π -orbital state to the edge magnetic moment of $\sim 0.3 \mu_B$ in a zigzag-edged GNR within the ferromagnetically ordered spin configuration [22].

As for the other model, we employ Lieb’s model [39], which predicts the appearance of net magnetization arising from small defects in sublattice of carbon hexagonal cell (*i.e.*, missing A and B sites underlying bipartite lattice). Even a small defect may still remain in actual pore edges. In order to elucidate the influence of such residual small-volume edge disorder on magnetism of GNM, we performed systematic first-principles calculations of magnetic properties of quasi-GNR structures (Figure 5a, corresponding to the inter-pore region) based on Lieb’s theorem [50], which introduces the slight disorder at the upper edge. Interestingly, the ground state of quasi-GNR structure turned out to be ferromagnetic in Figure 5b. The calculated net magnetic moment follows Lieb’s theorem with local moments up to $0.2 \mu_B/\text{edge atom}$ and depends on magnitude of the assumed edge disorder. These values agree fairly well with the value estimated from the GNR model.

Figure 5. (a) Structure of mono-hydrogen-terminated inter-pore graphene nanoribbon (GNR) region, which introduces small curvature (defects) with $\Delta_{AB} = 1$ (*i.e.*, the difference between the number of removed A and B sites of the graphene sublattices at zigzag edges) on the upper edge, used for first-principles calculations based on Lieb's theorem. The dark and white atoms are carbon and hydrogen, respectively; (b) Calculated spin-density distribution of quasi-GNR for (a), which gives the edge magnetic moment of $0.2 \mu_B$ to the lower edge.



Consequently, both models theoretically support that the observed ferromagnetism can originate from mono-hydrogenated zigzag nanopore edges. In order to determine which models are more relevant to the actual structures, observation of the pore edge atomic structures and number of the hydrogen atoms are indispensable. If the GNR model would be relevant, we have to assume presence of no defects at the pore edges. This seems to be realistic, because there are so many carbon atoms on one pore's edges and also so many nanopores in one GNM, as mentioned above. In contrast, if Lieb's theorem would be applicable, a small amount of defects should exist at the pore edges. However, following the above calculation, ferromagnetic spin alignment does not appear at the edge including defects in this case. This seems to be in poor agreement with the results of MFM observation mentioned above. Further experiments and comparison with theories are, therefore, indispensable.

2.2.2. Spin-Based Phenomena in MR Measurements of Few-Layer GNMs

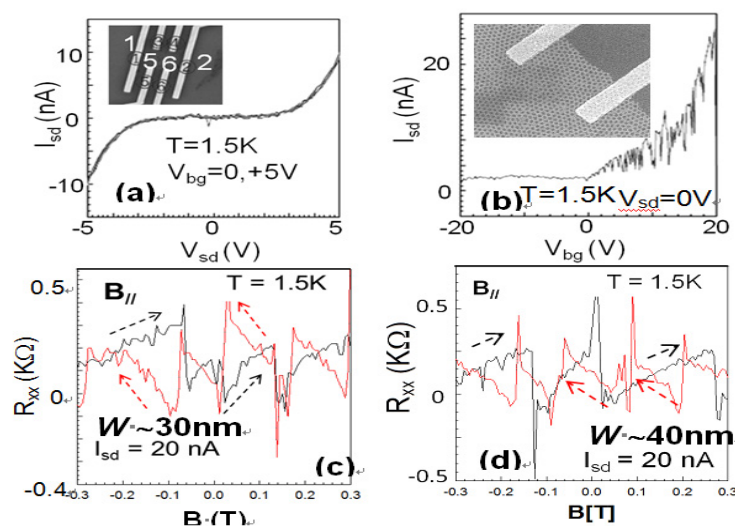
We have shown spontaneous spin polarization and ferromagnetism originating from the zigzag pore edges of monolayer GNMs. In contrast, the ferromagnetic GNMs demonstrated no clear electronic and MR features, because lithographical fabrication was used for formation of electrodes on the monolayer GNM. This method introduced contamination and disorder to the pore edges.

On the other hand, we previously confirmed periodic MR oscillations arising from electrons localizing at *H*-terminated pore edges in weak-ferromagnetic GNMs with ~ 10 layers, when magnetic fields were applied perpendicular to layers of the GNMs [42]. The observed oscillation period proved that the electron orbit localizing at the pore edges produced the oscillation with a period, which is shorter than those caused by free cyclotron-motion electrons due to applied fields. This result suggested that the contamination and disorder exist only around the most surface or the second-surface layers and the lower layers (e.g., the fifth layer) should mostly have no such influence. Thus, also in the present measurements, we measured MR behaviors of *H*-terminated GNMs with ~ 5 layers. Although magnitude of spin polarization at pore edges becomes weaker in the ~ 5 layer GNMs compared to that

of monolayer GNMs, we confirmed that the GNMs actually exhibited evident ferromagnetism in magnetization measurement and proved presence of polarized edge spins [38].

Typical drain current (I_{sd}) vs. drain voltage (V_{sd}) and I_{sd} vs. back-gate voltage (V_{bg}) behaviors of a ~ 5 layer ferromagnetic GNM are shown in Figures 6a and b, respectively. Figure 6a exhibits a strong zero-bias anomaly, which can be attributed to either single electron charging effect in narrow interpore GNR regions or high interface resistance between Au electrodes and GNM. Figure 6b shows an n -type semiconducting behavior also due to the narrow inter-pore GNR regions, which can introduce energy band gaps [32]. Because the band gaps are attributed to confinement of electrons into the one-dimensional space of the inter-pore regions (GNRs) [32], it is not controversial to assume the presence of zigzag pore edges.

Figure 6. (a) Typical I_{sd} vs. V_{sd} and (b) I_{sd} vs. V_{bg} behaviors measured between electrodes 1 and 2 (inset of (a)) in a ferromagnetic GNM with ~ 5 layers. It exhibits an n -type semiconducting behavior due to the narrow inter-pore GNR regions (Figure 1e). **Inset of (a):** SEM image of Hall pattern (six probes) formed on a GNM. MR (R_{xx}) between electrodes 5 and 6 was measured under a constant I_{sd} of 20 nA between electrodes 1 and 2. **Inset of (b):** FESEM image of a GNM around electrodes, which shows presence of array of nanopores; (c,d) MR (R_{xx}) behaviors under parallel fields in two different W samples with ~ 5 layers (i.e., (c) $W \sim 30$ nm and (d) ~ 40 nm, $\phi \sim 80$ nm is common). V_{bg} was set to +20 V. Arrows mean sequence of applied B (e.g., from -0.3 T to $+0.3$ T or from $+0.3$ T to -0.3 T).



MR (R_{xx}) behaviors of two different- W ferromagnetic GNMs ($W \sim 30$ nm and ~ 40 nm) for inset of Figure 6a-pattern under a constant current (I_{sd}) mode of a four probe measurement are shown in Figure 6c,d, when magnetic fields are applied in parallel with the GNM planes ($B_{||}$). They show saw-tooth like MR oscillations, in which MR monotonically increases with increasing fields, while it abruptly drops at a critical field and starts to increase again following a repeated manner. In Figure 6c for GNM with $W \sim 30$ nm, at $B < -0.05$ and $0.15 < B$, the oscillation periods are larger than those in the two oscillations around $B = 0$. The periods for all oscillations are the same for increasing and decreasing B . In contrast, in Figure 6d for GNM with $W \sim 40$ nm, the oscillation becomes ambiguous.

We call this saw-tooth like MR oscillation the spin pumping effect. The effect means a repeated cycle of gradual accumulation (increased number) of polarized spins and its abrupt emission (decreased number) at critical fields. No such anomalous behavior can be reported in any previous MR phenomena (e.g., ferromagnetic MR behavior, giant MR, tunnel MR, and spin valve effect), which is mentioned in the introduction.

In the present case, spin-polarized electrons localize at the pore edges under thermal equilibrium. However, under non thermal equilibrium caused by a constant current flow, the flat bands at the pore edges are modulated. Thus, some of the polarized electron-spins can no longer localize at the pore edges and flow through interpore bulk graphene regions. In our previous ~ 10 -layer GNMs with $W \sim 20$ nm [42], the spin pumping effect was not observed even under parallel fields, although MR oscillation arising from pore-edge localized electrons was found under perpendicular fields. This implies that enough inter-pore space W with bulk graphene regions for electron transport is indispensable for the spin flow and detection of the spin pumping effect.

Qualitatively possible interpretation for the present spin pumping effect is explained as follows. When the applied magnetic field is increased, the number of the localized polarized-spins increases at the pore edges. Moreover, other free electrons, which are flowing through bulk graphene regions among the pores, also tend to accumulate and polarize, when they locate close to the flat energy band of the pore edges. However, the accumulation of polarized-spins saturate at the pore edges. Then, the excess spins are abruptly emitted at a critical field, as parallel magnetic fields increase further, because the flat band is modulated in the GNM plane by increasing parallel fields more or less. After the emission of the accumulated excess spins, the flat band partially recovers near to the initial condition and the pore edges can allow the accumulation of further spins. Then, the MR starts to increase again, resulting in a repeated saw-tooth like feature. In Figure 6d for the GNM with $W \sim 40$ nm, the saw-tooth like oscillation becomes ambiguous, as mentioned above. This is qualitatively consistent with a decrease in ferromagnetism amplitude shown in Figure 3c, that is, reduction of amplitude of polarized spins at the pore edges in monolayer GNMs. This suggests the presence of optimized W values (e.g., 30 nm), which is the most suitable for appearance of spin pumping effect, with respect to the amount of pore edge polarized spins and its flow through array of nanopores.

The large W values induce spin flow through the interpore GNR regions, while it weakens magnitude of the polarized spins at the pore edges. In contrast, the small W values induce the amount of the polarized spins at the pore edges. It also obstructs sufficient spin flow via the interpore regions between electrodes and makes the detection of the spin flow difficult. Further optimization of the structures and clarifying the exact mechanism, therefore, are expected in the near future.

3. Conclusions

Recent advancement of the spin-based research of graphenes and our experiments for the edge-based spin phenomena have been reviewed. The former promises precise manipulation of coherent spins by applying electric fields. Avoiding the negative influence of substrate-based factors is crucial (e.g., by using h-BN substrate). In the latter, we successfully fabricated low-defected mono-layer GNMs by using a non-lithographic method (*i.e.*, using NPATs) and found the spontaneous emergence of large-amplitude ferromagnetism, only when pore edges of the GNMs were

H-terminated. Observed correlation between the inter-pore spacing and magnetism supported that it was attributed to electrons localizing at the zigzag pore-edges, which was in quantitative agreement with theories for pure GNR and defected-GNR models (Lieb's theorem). Moreover, the spin pumping effect was observed for fields applied in parallel with the GNM planes in few-layer GNMs with the optimized inter-pore spacing (~30 nm).

All-carbon spintronics is the key factor to realize magnetic rare-element free spintronic devices, which overcome the present material resource and environmental contamination problems. Strong spin coherence and its polarized edge spins of graphene must open the door to the novel spintronics with invisible, flexible, and ultra-light (wearable) features.

Acknowledgments

The author thank H. Yang and M. Chshiev for the first principle calculation, K. Fujita, Y. Hashimoto, E. Endo, Y. Iye, S. Katsumoto, M. Yamamoto, S. Tarucha for the device fabrication processes, T. Ando, T. Enoki, M. Koshino, J. Akimitsu, T. Muranaka, H. Aoki, S. Roche, X. Jia, and M. S. Dresselhaus for their fruitful discussions and encouragement. This work at Aoyama Gakuin was partly supported by a Grant-in-aid for Scientific Research (Basic research A: 24241046) in MEXT, a High-Technology Research Center Project for private universities in MEXT, and also AFOSR grant.

Conflicts of Interest

The authors declare no conflict of interest.

References

1. Baibich, M.N.; Broto, J.M.; Fert, A.; Van Dau, F.N.; Petroff, F.; Etienne, P.; Creuzet, G.; Friederich, A.; Chazelas, J. Giant magnetoresistance of (001)Fe/(001)Cr magnetic superlattices. *Phys. Rev. Lett.* **1988**, *61*, 2472.
2. Moodera, J.S.; Kinder, L.R.; Wong, T.M.; Meservey, R. Large magnetoresistance at room temperature in ferromagnetic thin film tunnel junctions. *Phys. Rev. Lett.* **1995**, *74*, 3273–3276.
3. Yuasa, S.; Nagahama, T.; Fukushima, A.; Suzuki, Y.; Ando, K. Giant room-temperature magnetoresistance in single-crystal Fe/MgO/Fe magnetic tunnel junctions. *Nat. Mat.* **2004**, *3*, 868–871.
4. Hayakawa, J.; Ikeda, S.; Lee, Y.M.; Matsukura, F.; Ohno, H. Effect of high annealing temperature on giant tunnel magnetoresistance ratio of magnetic tunnel junctions. *Appl. Phys. Lett.* **2006**, *89*, 232510.
5. Munekata, H.; Ohno, H.; von Molnar, S.; Segmüller, A.; Chang, L.L.; Esaki, L. Diluted magnetic III-V semiconductors, *Phys. Rev. Lett.* **1989**, *63*, 1849–1852.
6. Ohno, H.; Munekata, H.; Penney, T.; von Molnár, S.; Chang, L.L. Magnetotransport properties of *p*-type (In,Mn)As diluted magnetic III-V semiconductors. *Phys. Rev. Lett.* **1992**, *68*, 2664–2667.
7. Hai, P.N.; Ohya, S.; Tanaka, M.; Barnes, S.E.; Maekawa, S. Electromotive force and huge magnetoresistance in magnetic tunnel junctions. *Nature* **2009**, *458*, 489–492.

8. Lundeberg, M.B.; Yang, R.; Renard, J.; Folk, J.A. Defect-mediated spin relaxation and dephasing in graphene. *Phys. Rev. Lett.* **2013**, *110*, 156601.
9. Sun, Z.; Raji, A.O.; Zhu, Y.; Xiang, C.; Yan, Z.; Kittrell, C.; Samuel, E.L.G.; Tour, J.M. Large-area Bernal-stacked bi-, tri-, and tetralayer grapheme. *Nano* **2012**, *6*, 7615.
10. Tombros, N.; Jozsa, C.; Popinciuc, M.; Jonkman, H.T.; Van Wees, B.J. Electronic spin transport and spin precession in single graphene layers at room temperature. *Nature* **2007**, *448*, 571–574.
11. Tombros, N.; Tanabe, S.; Veligura, A.; Jozsa, C.; Popinciuc, M.; Jonkman, H.T.; Van Wees, B.J. Anisotropic spin relaxation in graphene. *Phys. Rev. Lett.* **2008**, *101*, 046601.
12. Abanin, D.A.; Morozov, S.V.; Ponomarenko, L.A.; Gorbachev, R.V.; Mayorov, A.S.; Katsnelson, M.I.; Watanabe, K.; Taniguchi, T.; Novoselov, K.S.; Levitov, L.S. Giant nonlocality near the Dirac point in graphene. *Science* **2011**, *332*, 328–330.
13. Murakami, S.; Nagaosa, N.; Zhang, S. Dissipationless quantum spin current at room temperature. *Science* **2003**, *301*, 1348–1351.
14. Kane, C.L.; Mele, E.J. Quantum spin hall effect in graphene. *Phys. Rev. Lett.* **2005**, *95*, 226801–226804.
15. Kane, C.L. Graphene and the quantum spin hall effect. *J. Mod. Phys. B* **2007**, *21*, 1155.
16. Schmidt, M.J.; Loss, D. Edge states and enhanced spin-orbit interaction at graphene/graphane interfaces. *Phys. Rev. B* **2010**, *81*, 165439.
17. Balakrishnan, J.; Koon, G.K.W.; Jaiswal, M.; Neto, A.H.C.; Özyilmaz, B. Colossal enhancement of spin-orbit coupling in weakly hydrogenated graphene. *Nat. Phys.* **2013**, *9*, 284–287.
18. Nakada, K.; Fujita, M.; Dresselhaus, G.; Dresselhaus, M.S. Edge state in graphene ribbons: Nanometer size effect and edge shape depend. *Phys. Rev. B* **1996**, *54*, 17954–17961.
19. Fujita, M.; Wakabayashi, K.; Nakada, K.; Kusakabe, K. Peculiar localized state at zigzag graphite edge. *J. Phys. Soc. Jpn.* **1996**, *65*, 1920–1923.
20. Kusakabe, K.; Maruyama, M. Magnetic nanographite. *Phys. Rev. B* **2003**, *67*, 092406.
21. Okada, S.; Oshiyama, A. Magnetic Ordering in Hexagonally Bonded Sheets with First-Row Elements. *Phys. Rev. Lett.* **2001**, *87*, 146803.
22. Lee, H.; Son, Y.; Park, N.; Han, S.; Yu, J. Magnetic ordering at the edges of graphitic fragments: Magnetic tail interactions between the edge-localized states. *Phys. Rev. B* **2005**, *72*, 174431.
23. Veiga, R.G.A.; Miwa, R.H.; Srivastava, G.P. Quenching of local magnetic moment in oxygen adsorbed graphene nanoribbons. *J. Chem. Phys.* **2008**, *128*, 201101.
24. Lee, H.; Park, N.; Son, Y.; Han, S.; Yu, J. Ferromagnetism at the edges of the stacked graphitic fragments: An *ab initio* study. *Chem. Phys. Lett.* **2004**, *398*, 207–211.
25. Enoki, T.; Takai, K. The edge state of nanographene and the magnetism of the edge-state spins. *Sol. Stat. Comm.* **2009**, *149*, 1144–1150.
26. Son, Y.; Cohen, M.L.; Louie, S.G. Energy gaps in graphene nanoribbons. *Phys. Rev. Lett.* **2006**, *97*, 216803.
27. Yang, L.; Park, C.; Son, Y.; Cohen, M.L.; Louie, S.G. Quasiparticle energies and band gaps in graphene nanoribbons. *Phys. Rev. Lett.* **2007**, *99*, 186801.
28. Shima, N.; Aoki, H. Electronic structure of super-honeycomb systems: A peculiar realization of semimetal/semiconductor classes and ferromagnetism. *Phys. Rev. Lett.* **1993**, *71*, 4389–4392.

29. Rosser, J.F.; Palacios, J.J. Magnetism in Graphene Nanoislands. *Phys. Rev. Lett.* **2007**, *99*, 177204.
30. Jia, X.; Hofmann, M.; Meunier, V.; Sumpter, B.G.; Campos-Delgado, J.; Romo-Herrera, J.M.; Son, H.; Hsieh, Y.; Reina, A.; Kong, J. Controlled formation of sharp zigzag and armchair edges in graphitic nanoribbons. *Science* **2009**, *323*, 1701–1705.
31. Girit, Ç.Ö.; Meyer, J.C.; Erni, R.; Rossell, M.D.; Kisielowski, C.; Yang, L.; Park, C.; Crommie, M.F.; Cohen, M.L.; Louie, S.G. Graphene at the edge: Stability and dynamics. *Science* **2009**, *323*, 1705–1708.
32. Shimizu, T.; Haruyama, J.; Marcano, D.C.; Kosinkin, D.V.; Tour, J.M.; Hirose, K.; Suenaga, K. Large intrinsic energy bandgaps in annealed nanotube-derived graphene nanoribbons. *Nat. Nanotech.* **2011**, *6*, 45–50.
33. Han, M.Y.; Brant, J.C.; Kim, P. Electron transport in disordered graphene nanoribbons. *Phys. Rev. Lett.* **2010**, *104*, 056801.
34. Wang, X.; Ouyang, Y.; Li, X.; Wang, H.; Guo, J.; Dai, H. Room-temperature all-semiconducting sub-10-nm graphene nanoribbon field-effect transistors. *Phys. Rev. Lett.* **2008**, *100*, 206803.
35. Krauss, B.; Nemes-Incze, P.; Skakalova, V.; Biro, L.P.; von Klitzing, K.; Smet, J.H. Raman scattering at pure graphene zigzag edges. *Nano Lett.* **2010**, *10*, 4544–4548.
36. Bai, J.; Zhong, X.; Jiang, S.; Huang, Y.; Duan, X. Graphene nanomesh. *Nat. Nanotech.* **2010**, *5*, 190–194.
37. Son, Y.W.; Cohen, M.L.; Louie, S.G. Half-metallic graphene nanoribbons. *Nature* **2006**, *444*, 347–349.
38. Otani, M.; Koshino, M.; Takagi, Y.; Okada, S. Intrinsic magnetic moment on (0001) surfaces of rhombohedral graphite. *Phys. Rev. B* **2010**, *81*, 161403 (R).
39. Yang, H.; Chshiev, M.; Boukhvalov, D.W.; Waintal, X.; Roche, S. Inducing and optimizing magnetism in graphene nanomeshes. *Phys. Rev. B* **2011**, *84*, 214404.
40. You, Y.M.; Ni, Z.H.; Yu, T.; Shen, Z.X. Edge chirality determination of graphene by Raman spectroscopy. *Appl. Phys. Lett.* **2008**, *93*, 163112.
41. Soriano, D.; Leconte, N.; Ordejón, P.; Charlier, J.; Palacios, J.; Roche, S. Magnetoresistance and magnetic ordering fingerprints in hydrogenated graphene. *Phys. Rev. Lett.* **2011**, *107*, 016602.
42. Shimizu, T.; Nakamura, J.; Tada, K.; Yagi, Y.; Haruyama, J. Magnetoresistance oscillations arising from edge-localized electrons in low-defect graphene antidot-lattices. *Appl. Phys. Lett.* **2012**, *100*, 023104.
43. Tada, K.; Hashimoto, T.; Haruyama, J.; Yang, H.; Chshiev, M. Spontaneous spin polarization and spin pumping effect on edges of graphene antidot lattices. *Phys. Status Solidi* **2012**, *249*, 2491–2496.
44. Ning, G.; Xu, C.; Hao, L.; Kazakova, O.; Fan, Z.; Wang, H.; Wang, K.; Gao, J.; Qian, W.; Wei, F. Ferromagnetism in nanomesh graphene. *Carbon* **2013**, *51*, 390–396.
45. Nair, R.R.; Sepioni, M.; Tsai, I.; Lehtinen, O.; Keinonen, J.; Krasheninnikov, A.V.; Thomson, T.; Geim, A.K.; Grigorieva, I.V. Spin-half paramagnetism in graphene induced by point defects. *Nat. Phys.* **2012**, *8*, 199–202.

46. Rao, S.S.; Jammalamadaka, S.N.; Stesmans, A.; Moshchalkov, V.V.; Van Tol, J.; Kosynkin, D.V.; Higginbotham-Duque, A.; Tour, J.M. Ferromagnetism in graphene nanoribbons: Split versus oxidative unzipped ribbons. *Nano Lett.* **2012**, *12*, 1210–1217.
47. Prével, B.; Benoit, J.-M.; Bardotti, L.; Mélinon, P.; Ouerghi, A.; Lucot, D.; Bourhis, E.; Gierak, J. Nanostructuring graphene on SiC by focused ion beam: Effect of the ion fluence. *Appl. Phys. Lett.* **2011**, *98*, 83116.
48. Takesue, I.; Haruyama, J.; Kobayashi, N.; Chiashi, S.; Maruyama, S.; Sugai, T.; Shinohara, H. Superconductivity in entirely end-bonded multiwalled carbon nanotubes. *Phys. Rev. Lett.* **2006**, *96*, 057001.
49. Niimi, Y.; Matsui, T.; Kambara, H.; Tagami, K.; Tsukada, M.; Fukuyama, H. Scanning tunneling microscopy and spectroscopy of the electronic local density of states of graphite surfaces near monoatomic step edges. *Phys. Rev. B* **2006**, *73*, 085421.
50. Asano, H.; Muraki, S.; Endo, H.; Bandow, S.; Iijima, S. Strong magnetism observed in carbon nanoparticles produced by the laser vaporization of a carbon pellet in hydrogen-containing Ar balance gas. *J. Phys.* **2010**, *22*, 334209.

© 2013 by the authors; licensee MDPI, Basel, Switzerland. This article is an open access article distributed under the terms and conditions of the Creative Commons Attribution license (<http://creativecommons.org/licenses/by/3.0/>).